Original Research Article

Virtual Design of Novel Coumarinyl-Substituted Sulfonamide Inhibitors of Carbonic Anhydrase II as Potential Drugs against Glaucoma

ABSTRACT

(1) Background: We have carried out virtual design of coumarinyl-substituted sulfonamides (CSAM) analogs as inhibitors of human carbonic anhydrase II (*h*CA II) endowed with favorable predicted pharmacokinetic profiles and potential therapeutic effects against glaucoma. **(2) Methods**: modifying *in situ* the x-ray structure of 2-(7-methoxy-2-oxo-2H-chromen-4-yl)-N-(4-sulfamoyl-phenyl)-acetamide (CSAM0)-*h*CA II complex (PDB entry 3ML2), permitted 3D models of *h*CA II-CSAMx complexes preparation for a TS of 14 CSAMs the experimental activities of which are available in the literature (IC_{50}^{exp}). Active bound conformation of the CSAM1-14 assessment led to linear correlation between computed enthalpy of *h*CA II-CSAMx complexes formation in gas phase ($\Delta\Delta H_{MM}$) with the IC_{50}^{exp}. Moreover, considering the solvation and ligand loss of entropy upon binding led to a superior QSAR model where a better linear correlation is established between calculated GFE ($\Delta\Delta G_{com}$) and IC_{50}^{exp}. The successive 3D-pharmacophore (PH4) built from CSAMs active conformations helped to virtually screen CSAM populating a sulfonamides scaffolds virtual combinatorial library (VCL), focused by Lipinski's rule-of-five to reach novel CSAMs. **(3) Results**: Enthalpy QSAR model: pIC_{50}^{exp} = -0.068×$\Delta\Delta H_{MM}$ + 7.722, R^2 = 0.82; GFE QSAR model: pIC_{50}^{exp} = - 0.061× $\Delta\Delta G_{com}$ + 7.647, R^2 = 0.92 and PH4 model: pIC_{50}^{exp} = 1.095×pIC_{50}^{pre} – 0.680, R^2 = 0.87. The VCL of more than 1,500,625 CSAMs was lowered to 865,670 drug likely compounds by the Lipinski's rule (except the restriction $M_w \leq 500$ g/mol). The three-point PH4-based screening identified 81 novel CSAMs with predicted IC_{50}^{pre} reaching 78-times better than CSAM1 potency (IC_{50}^{exp} = 23 nM). Computed pharmacokinetic profile of the new candidates showed enhanced cell membrane permeability and high human oral absorption compared to current anti-glaucoma agents. **(4) Conclusions**: Combination of QSAR models of the CSAMs' affinity to the *h*CA II, pharmacophore model, and ADME profile guided to the sulfonamides inhibitors identification and helped to *in silico* screen VCL sulfonamides scaffold bearing analogs and allowed emerging of novel more potent compounds with predicted IC_{50} and favorable pharmacokinetic profiles.

KEYWORDS**:** Coumarin; glaucoma; sulfonamide; carbonic anhydrase II; molecular modeling; QSAR models; pharmacophore; virtual combinatorial library; *in silico* screening; ADME properties prediction

Abbreviations

2D	Two-dimensional
3D	Three-dimensional
AAZ	Acetazolamide
ADME	Absorption, distribution, metabolism, and excretion
AHO	Hydroxamic acids inhibitors
CA II	Carbonic Anhydrase II
CAIs	Carbonic Anhydrase Inhibitors
CAMD	Computer-aided molecular design
CSAM	Coumarinyl-substituted sulfonamides
Eint	MM enzyme–inhibitor interaction energy per residue
$\Delta\Delta G_{com}$	Relative complexation GFE
GFE	Gibbs free energy
$\Delta\Delta G_{sol}$	Relative solvation GFE
HBA	Hydrogen bond Acceptor
HBD	Hydrogen bond Donor
H_{MM}	Enthalpy component of GFE
HOA	Human oral absorption
HYD	Hydrophobic
HYDA	Hydrophobic Aliphatic
IC_{50}	Half-maximal inhibitory concentration
IE	Interaction energy
LHP	Large hydrophobic pocket
LOO	Leave-one-out cross-validation
MM	Molecular mechanics
MM-PB	Molecular mechanics–Poisson–Boltzmann
PDB	Protein Data Bank
PH4	Pharmacophore
QSAR	Quantitative structure–activity relationships
RMSD	Root-mean square deviation
SAR	Structure–activity relationships
SA	Sulfanilamide
TS	Training set
VS	Validation set
WHO	World Health Organization

Introduction

Glaucoma is a major cause of visual impairment and blindness worldwide being responsible for 64.3 million blind individuals in 2013, projected to reach 76 million in 2020 [1]. In October 2019 the World Health Organization (WHO) launched the first report on vision that estimates around 76 million people 40 to 80 years old with glaucoma in 2020 [2] and states: "At least 2.2 billion people have vision impairment or blindness, of which over 1 billion cases could have been prevented or have yet to be addressed" [2]. Glaucoma is a chronic degenerative optic

neuropathy where the loss of retinal ganglion cells results in an irreversible damage of the optic nerve head, progressive loss of visual function and blindness. High intraocular pressure (IOP) is the major and only known modifiable risk factor of glaucoma. Therapy aims at lowering the IOP by means of laser surgical treatment or therapeutics. Lowering of the IOP is achieved by administration of drugs such as latanoprostene bunod (LBN), netarsudil, and fixed combination netarsudil/ latanoprost (FCNL) as the first-line treatment, since the damage progression stops as the pressure is lowered by 30%–50% [3, 4]. Unfortunately, early detection and treatment is not easy since early stages of glaucoma are asymptomatic until 20%–50% of the corresponding retinal ganglion cells are lost [5, 6]. Nowadays artificial intelligence reveals as a central tool for early diagnosis and management of glaucoma, when applied in the image-based ophthal-mology field [7].

Carbonic anhydrases (CAs) are metalloenzymes expressed in all living organism, catalyzing the reversible hydration of carbon dioxide (CO_2) to bicarbonate in the anterior uvea of the eye. Their function *in vivo* is to catalyze reversible hydration of CO_2 to form bicarbonate (HCO_3^-) and proton and *vice versa* [8]. This reaction is the basis of certain physiological and homeostatic functions such as respiration, pH regulation, calcification, bone resorption, gas exchange and biosynthetic and tumorigenic processes [9, 10]. For decades CAs have been known as validated drug targets for a wide range of diseases and used in the design antiglaucoma, antiepileptics, antiobesity, anticancer, and diuretic agents [11, 12, 13, 14, 15, 16].

The crystallographic structure of carbonic anhydrase II (CA II) was determined by X-ray crystallography for the first time in 1972 [17]. Its conically shaped active site has at its peak a zinc ion II which is coordinated by three histidine residues His94, His96, and His119. The CA II has an amphiphilic active site because of the presence of a hydrophobic pocket and a hydrophilic pocket.

Carbonic anhydrase isoenzymes inhibitors (CAIs) address many diseases and the most potent among them are sulfonamides [18, 19]. The human carbonic anhydrase isozyme II (*h*CA II) shows a high catalytic activity and very high affinity for sulfonamides. The first antiglaucoma CAI, namely acetazolamide (AAZ), a powerful carbonic anhydrase inhibitor [20], approved in 1954, is still in use nowadays but in very limited cases only [21,22, 23]. More recent CAIs such as dorzolamide (DZA), brimonidine and brinzolamide (BRZ), Scheme 1, are associated with various side effects, adverse reactions and pH lowering of eye solution …, making the design of high-affinity, water soluble and neutral pH sulfonamide CAIs difficult [24,25,26,27,28].

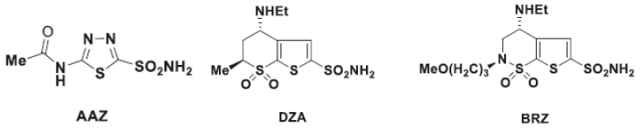

Scheme 1. Chemical structures of sulfonamides: acetazolamide (AAZ), dorzolamide (DZA), brinzolamide (BRZ).

Well-documented and recent reviews about *h*CA II inhibition by sulfonamides reveal a common pharmacophore including a zinc-binding group (ZBG), a scaffold, a hydrophilic linker (at one side of the active site) and a hydrophobic tail (at the other side) [29]. Scheme 2 summarizes a comparative analysis of two main scaffolds such as the thiadiazole of AAZ and benzene keeping in mind that a coumarin at that position resulted in the least active analog [29]. Similarly, mono and polycyclic tails, such as phtalimide, substituted benzene, phenylsulfone and coumarin or other bulky hydrophobic groups, retain the same range of binding affinity. Almost a decade ago coumarins have emerged as novel class of natural product (NP) non-zinc mediated CA inhibitors with active site entrance occlusion mechanism supported by stacking interactions with Phe131 and a network of polar and hydrogen bonds (HB) with Glu238 and Asn67. Despite a favorable pharmacokinetic profile common to NPs, the *h*CA II inhibition potency could not overcome the two-digit nanomolar concentration range (K_i ≥ 60 nM) [30]. Sulfonamides are potent *h*CA II inhibitors reaching the low nanomolar range (< 1 nM) but are limited by various undesired side-effects. On the other hand, coumarins are "safe" but 60 to 100-fold less potent. Coumarinyl-substituted sulfonamide CAIs are thought to combine the zinc mediated mechanism represented by the benzene sulfamide moiety and the active site entrance occlusion introduced by the coumarin through stacking interactions with the Phe131. This combination resulted in reported potency improved to a one-digit nanomolar CAIs (K_i = 9 nM) [27, 31, 32]. Besides the *h*CA II affinity improvement, to secure favorable pharmacokinetic profiles of new CAIs is to resort to naturally occurring sulfonamides. Due to lack of experimental ADME data computed descriptors such as blood-brain barrier permeability, Caco-2 cell membrane permeability, human oral absorption, etc., were used to estimate their ADME profiles [33].

Taking advantage of known inhibitory potencies of sulfonamides (Scheme 2) and substituents of the coumarin on one side and of the amino linker on the other side of the molecules, novel sulfonamide analogs with predicted *h*CA II inhibitory activities in the subnanomolar concentration range were proposed.

We virtually design here novel CSAMs originating from a TS of 14 reported CSAM hybrids and their IC_{50}^{exp} [32]. We have based our design of new analogues on this set and predicted the inhibitory potencies of designed CSAM with help of 3D structural model of the *h*CA II, computed

standard GFE of *h*CA II-CSAM complex formation (ΔG_{com}), QSAR, and the enzyme-inhibitor (E:I) interactions analysis. Relative changes in ΔG_{com} were correlated in a linear regression QSAR model with the IC_{50}^{exp} [24].

Each complex was carefully built by *in situ* modification of the reference crystal structure of *h*CA II (3ML2) [32] in complex with a coumarinyl-substituted sulfonamide, the 2-(7-methoxy-2-oxo-2H-chromen-4-yl)-N-(4-sulfamoylphenyl) -acetamide CSAM0 (Figure 1). The 3D models of inhibitors bound to *h*CA II, QSAR and pharmacophore (PH4) models derived for the training set compounds provided the necessary structural information needed to improve inhibitor interactions at individual pockets of the CA II active site. PH4-based screening of enumerated VCL of CSAM analogues led to novel potent CSAM, predicted to be more potent than the best TS CSAM1 (IC_{50}^{exp} = 23 nM).

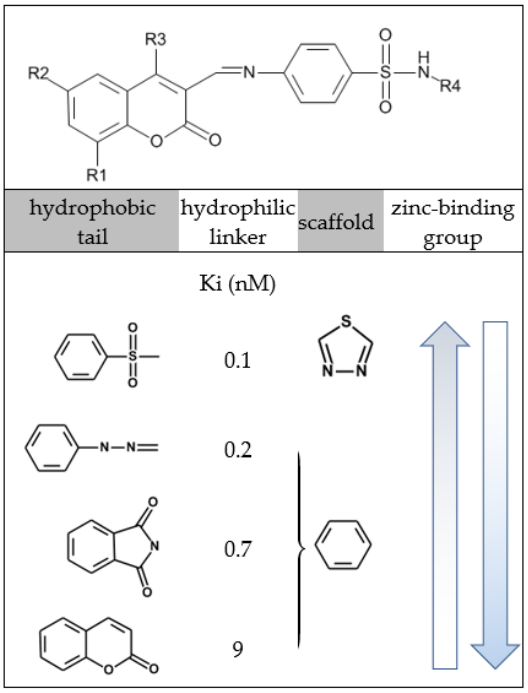

Scheme 2. Inhibitory activity and pharmacokinetic profile of CSAM inhibitors of *h*CA II.

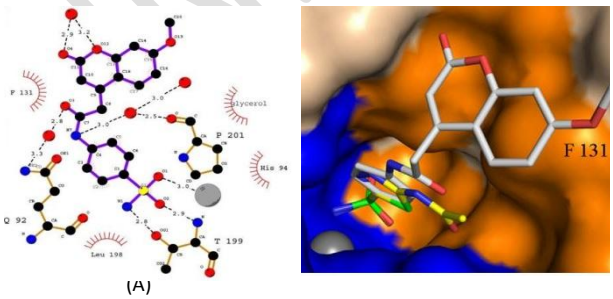

(A) (B)

Figure 1. Schematic of *h*CA II– CSAM0 interactions [34]. (A) Hydrophobic contacts are indicated by red hash marks, (B) Overall view of *h*CA II - CSAM0, superposed onto acetazolamide (AAZ) (PDB code 3HS4) [34]. Note that both compounds follow the same trajectory out of the active site with the extended conformation of the coumarin heterocycle ring tilted towards the benzene ring with an edge-to-face interaction with the side chain of the Phe131. The *h*CA II is represented by molecular surface (bulk solvent accessible area, light pink; hydrophilic and hydrophobic regions of the active site, blue and orange, respectively). CSAM0 (gray) and AAZ (yellow) are represented by stick model. Non-carbon atoms of both compounds are colored [32].

Materials and Methods

2.1. Training sets

Chemical structures and biological activities (IC_{50}^{exp}) of the reported [32] seventeen (14 TS and 3 VS) 4-[(2-Oxo-2H-chromen-3-ylmethylene)-amino]-benzene-sulfonamide inhibitors of *h*CA II range from 23 to 217 nM, broad enough to build a reliable QSAR model.

2.2. Model building

Three-dimensional (3D) molecular models of enzyme–inhibitor (E-I) complexes *h*CA II-CSAMx, free enzyme *h*CA II and free inhibitors CSAMx were prepared from high-resolution (2.2 Å) crystal structure of a reference complex containing the compound 2-(7-methoxy-2-oxo-2H-chromen-4-yl)- N-(4-sulfamoylphenyl)-acetamide (CSAM0, Figure 1) [34] bound to the *h*CA II (Protein Data Bank entry code 3ML2) using Insight-II molecular modeling program [35]. The structures were processed according to a procedure des-cribed earlier and successfully used to design peptidomi-metic, hydroxynaphthoic, thymidine, triclosan, pyrrolidine carboxamide, nitriles, and chalcone-based viral, bacterial, and protozoal enzyme inhibitors [36, 37, 38, 39, 40, 41, 42, 43, 44].

2.3. Molecular mechanics

Enzyme, Inhibitor and their complexes MM energies were computed as described in ref. [45, 46].

2.4. Conformational search

Free inhibitor conformations were derived from their bound conformations in the E-I complexes by gradual relaxation to the nearest local energy minimum as described earlier [45].

2.5. Solvation Gibbs free energies

The solvation free energy G_{sol} was described earlier [45, 47].

2.6. Calculation of binding affinity and QSAR model

The calculation of binding affinity expressed as complexation GFE has been described fully earlier [45].

2.7. Interaction energy

The calculation of MM interaction energy (E_{int}) between enzyme residues and the inhibitor was performed as described earlier [45].

2.8. Pharmacophore generation

Bound conformations as described earlier [45] of inhibitors taken from the models of E-I complexes were used for constructing of 3D-QSAR pharmacophore (PH4) by means of Catalyst HypoGen algorithm [48] in Discovery Studio [49].

3-Results and Discussion

3.1. Training and validation sets

The TS of 14 CSAMs and VS of 3 analogs (Table 1) belong to a homogeneous series of *h*CA II inhibitors the experimental potencies of which come from only one laboratory [32]. The seventeen CSAMs differ by substitution at four positions R1 to R4 of the coumarin heterocycle and sulfonamide group as listed in Table 1. The IC_{50}^{exp} (23 nM ≤ IC_{50}^{exp} ≤ 217 nM) [32] cover relatively broad range in order to elaborate a QSAR model with robust predictability. The ratio "TS size / VS size" remains a critical point of adequate splitting but remains limited by the count of reported compounds [50].

Table 1. TS (CSAM1-14) and VS (CSAM15-17) of *h*CA II inhibitors used to elaborate QSAR models of CSAM binding to *h*CA II [32]. Experimental inhibitory potencies (IC_{50}^{exp}) are taken from ref. [32]. The R1 to R4-groups of the CSAM scaffold are numbered 1 to 9 in the first part of the Table.

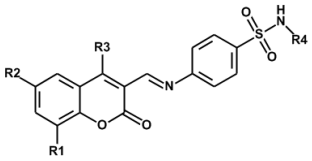

Substituents	**1**	**2**	**3**	**4**	**5**
	----H	----Cl			
Substituents	**6**	**7**	**8**	**9**	
	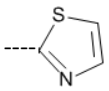	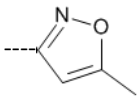	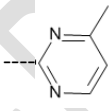	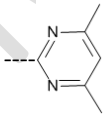	

Training set	CSAM 1	CSAM2	CSAM 3	CSAM 4	CSAM 5	CSAM 6	CSAM 7
$\#R_1\text{-}\#R_2\text{-}\#R_3\text{-}\#R_4$	1-1-2-9	1-1-2-4	1-1-2-6	1-1-2-5	1-1-2-7	1-1-2-8	4-4-2-5
IC_{50}^{exp}(nM)	23	33	58	85	26	51	112

Training set	CSAM 8	CSAM 9	CSAM 10	CSAM 11	CSAM 12	CSAM 13	CSAM 14
$\#R_1\text{-}\#R_2\text{-}\#R_3\text{-}\#R_4$	1-3-2-7	4-4-2-5	4-4-2-9	4-4-2-7	1-3-2-1	1-3-2-5	1-3-2-9
IC_{50}^{exp}(nM)	217	103	173	173	88	121	100

Validation set	CSAM15	CSAM16	CSAM17
$\#R_1\text{–}\#R_2\text{-}\#R_3\text{-}\#R_4$	4-4-2-6	1-3-2-7	1-3-2-8
IC_{50}^{exp}(nM)	122	141	61

3.1. Quantitative Structure-Activity Relationships (QSAR) model

Each of the seventeen (14 TS and 3 VS) *h*CA II - CSAM1-17 complexes was constructed by *in situ* modificating the reference x-ray crystal structure (PDB entry 3ML2 [32]) and followed by gas phase optimization as detailed in the Methods section. The relative GFE upon each of the 17 *h*CA II - CSAMx complex formation ($\Delta\Delta G_{com}$) was calculated and presented in Table 2 along with the three components of this unique QSAR descriptor namely the enthalpy of complexation in the gas phase $\Delta\Delta H_{MM,}$ the ligand loss of entropy $\Delta\Delta TS_{vib}$ and the Poisson Boltzmann solvation free energy $\Delta\Delta G_{sol}$, as defined in Equation (7), for the coumarinyl-substituted sulfonamides [32]. From the elaborated QSAR statistics the reported CSAMs' pIC_{50}^{exp} (pIC_{50}^{exp} = $-\log_{10}(IC_{50}^{exp})$ [32] correlates linearly with calculated $\Delta\Delta G_{com}$ (Equation (8), Table 2). This significant correlation relationship let identify the CSAMs active bound conformation at the *h*CA II binding site and generate the *h*CA II inhibition PH4 pharmacophore. Analysis of the enthalpy of complexation in the gas phase $\Delta\Delta H_{MM}$ by correlating it with the pIC_{50}^{exp} leads to a deeper insight into the ligand affinity towards the enzyme. The validity of this linear correlation (Table 3, Eq. A) permitted assessment of the significance of the strength of E-I interactions ($\Delta\Delta H_{MM}$) when solvation and ligand loss of entropy upon binding to *h*CA II are neglected, explaining about 82% of the pIC_{50}^{exp} variation and underlining the enthalpic contribution's role to the CSAMs inhibitors binding to *h*CA II. In the same way a better structural descriptor, GFE of the *h*CA II - CSAMx complex formation including $\Delta\Delta H_{MM}$, $\Delta\Delta TS_{vib}$ and $\Delta\Delta G_{sol}$, (Table 3, Eq. B) led to higher regression correlation coef-ficients R^2, R^2_{xv} and Fischer F-test and suggests a deeper quantitative structure-activity relationship. Thus, *h*CA II - CSAMx complexes 3D models information can lead to

reliable prediction CSAM analogs' IC_{50} from the QSAR model B, Table 3.

Table 2. GFE (binding affinity) and its components for TS CSAM1-14 and VS inhibitors CSAM15-17 of *h*CA II inhibitors [32].

Training Set [a]	M_w [b]	$\Delta\Delta H_{MM}$ [c]	$\Delta\Delta G_{sol}$ [d]	$\Delta\Delta TS_{vib}$ [e]	$\Delta\Delta G_{com}$ [f]	IC_{50}^{exp} [h]
CSAM1*	**468**	**0.0**	**0.0**	**0.0**	**0.0**	**23**
CSAM2	362	7.0	-2.7	0.5	**3.8**	33
CSAM3	445	7.8	-2.2	-0.5	**6.1**	58
CSAM4	404	11.5	-0.2	2.2	**9.1**	85
CSAM5	443	2.5	-1.0	-0.6	**2.0**	26
CSAM6	454	5.6	-1.2	-2.4	**6.8**	51
CSAM7	474	12.6	9.9	9.7	**12.8**	112
CSAM8	457	11.1	3.2	-1.0	**15.4**	217
CSAM9	516	11.1	10.8	9.3	**12.6**	103
CSAM10	580	14.3	9.5	9.6	**14.2**	173
CSAM11	555	11.9	10.0	7.5	**14.3**	173
CSAM12	376	11.4	-1.8	1.9	**7.7**	88
CSAM13	459	10.7	-3.4	-1.4	**8.7**	121
CSAM14	482	10.7	-0.5	-0.2	**10.4**	100
Validation set	M_w [b]	$\Delta\Delta H_{MM}$ [c]	$\Delta\Delta G_{sol}$ [d]	$\Delta\Delta TS_{vib}$ [e]	$\Delta\Delta G_{com}$ [f]	$\frac{pIC_{50}^{pre}}{pIC_{50}^{exp}}$ [g]
CSAM15	418	12.6	10.0	9.8	**12.8**	1.0208
CSAM16	474	8.7	2.1	-0.8	**11.7**	1.0245
CSAM17	468	5.7	1.0	-0.6	**7.3**	1.0037

[a] for the chemical structures of TS CSAMs see Table 1; [b] M_w inhibitors' molar mass in g.mol^{-1}; [c] $\Delta\Delta H_{MM}$ *see Abbreviations*; [d] $\Delta\Delta G_{sol}$ *see Abbreviations*; [e] -$\Delta\Delta TS_{vib}$ *see Abbreviations*; [f] $\Delta\Delta G_{com}$ *see Abbreviations*; [g] IC_{50}^{exp} in nM (*see Abbreviations*) of *h*CA II inhibition from ref. [30]; [h] ratio of predicted and experimental potency $pIC_{50}^{pre}/pIC_{50}^{exp}$ ($pIC_{50}^{pre} = -log_{10}IC_{50}^{pre}$) was predicted from computed $\Delta\Delta G_{com}$ using the regression equation for *h*CA II shown in Table 3, B. [c, d, e, f]: all in kcal.mol^{-1}.

Table 3. Correlation of computed GFE $\Delta\Delta G_{com}$, its enthalpic component $\Delta\Delta H_{MM}$, and experimental pIC_{50}^{exp} of *h*CA II inhibitors CSAMs [32].

Statistical data of regression	A	B
$pIC_{50}^{exp} = -0.068\times\Delta\Delta H_{MM} + 7.722$ (A)		
$pIC_{50}^{exp} = -0.061\times\Delta\Delta G_{com} + 7.647$ (B)		
Number of compounds *n*	14	14
Squared correlation coefficient of regression R^2	0.82	0.92
LOO cross-validated squared correlation coef. R_{xv}^2	0.80	0.90
Standard error of regression σ	0.13	0.08
Statistical significance of regression, Fischer *F-test*	53.6	149.2
Level of statistical significance $\propto$	>98%	>98%
Range of activities IC_{50}^{exp} (nM)	23 - 217	

The statistical quality of both correlations represented their equations (A) and (B) respectively (see plot on Figure 2) is described by data listed in Table 3. The ratio $pIC_{50}^{pre}/pIC_{50}^{exp} \approx 1$ ($pIC_{50}^{pre} = -0.061\times\Delta\Delta G_{com} + 7.647$, (eq. B)) for the VS CSAM15-17 confirms the substantial predictability of the QSAR model (Table 2). Accordingly, the regression eq. B (Table 3) and calculated $\Delta\Delta G_{com}$ GFEs can be lead to prediction of the *h*CA II inhibition activity IC_{50}^{pre} for any CSAM analogs, sharing the binding conformation of the TS coumarinyl-substituted sulfonamides CSAM1-14.

A

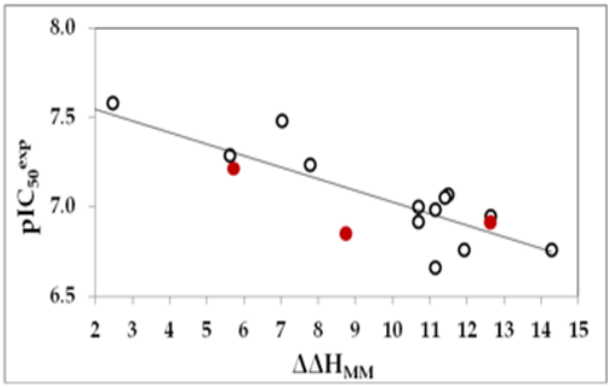

B

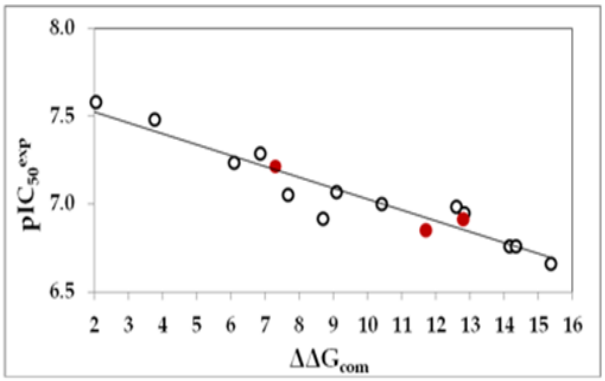

Figure 2. (A) Plot of correlation between pIC_{50}^{exp} and relative enthalpic contribution to the GFE $\Delta\Delta H_{MM}$ [kcal.mol^{-1}]; (**B**) similar plot for relative complexation GFE of the CA II- CSAMx complex formation $\Delta\Delta G_{com}$ [kcal.mol^{-1}] of the training set. The validation set data points are shown in red color.

3.2. Binding mode of inhibitors

3D *h*CA II - CSAMx interactions retrieved from the crystallographic data of *h*CA II - CSAM1 complex [30] suggest that CSAMs are *h*CA II specific inhibitors. As displayed in Figure 3, in the catalytic site I the coumarin heterocyclic ring of the inhibitor forms a π –π stacking interaction with Phe131 [34, 51] and hydrophobic interactions with residue Gln92 known to interact with other classes of inhibitors (sulfonamides, sulfamates, coumarins) from previous X-ray crystallographic work [30 ,52, 53] as well as Val121, Val135, Leu141 and Val143. In the hydrophobic site II, the phenyl ring occupies the hydrophobic substrate pocket, where nonpolar residues' lateral chains are present: Pro202 [34] and Trp209. In addition, it makes a stacking interaction with His94. In the hydrophilic site III, one oxygen of the secondary SO_2 moiety of inhibitor made a hydrogen bond with the OH of Thr199, an amino acid conserved in all α-CAs and critically important for the catalytic cycle of these enzymes [38] and NH group made a hydrogen bond with Thr200 a key interaction reported recently [34, 54]. The pyrimidine moiety of inhibitor makes π –π stacking interactions with His94 and His96.

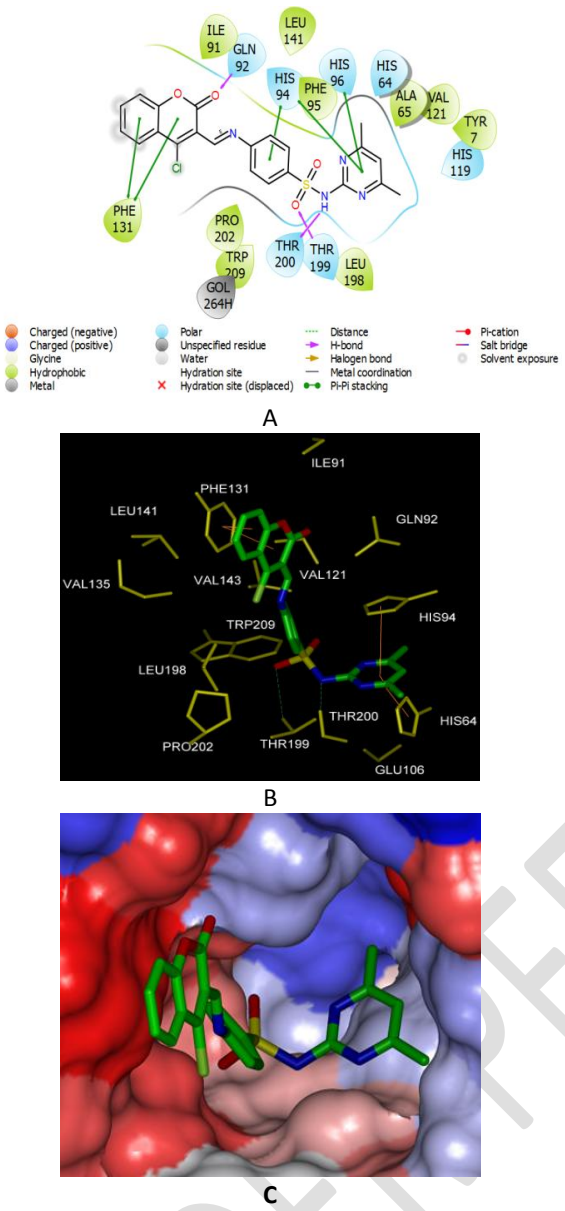

Figure 3. (A) 2D schematic interaction diagram of the most potent inhibitor CSAM1 [32] at the active site of hCA II. (B) 3D structure of the hCA II active site with bound inhibitor CSAM1. (C) Connolly surface of hCA II binding site occupied by (most active TS inhibitor). Surface coloring legend: red - hydrophobic, blue - hydrophilic and white - intermediate.

3.3. Interaction Energy

The molecular mechanics interaction energy (IE, ΔE_{int}) diagram displaying the global E-I energy and its breakdown into each *h*CA II active site residue contribution. Since E_{int} diagram reveals each inhibitor moiety interacting with one or a group of *h*CA II active site residues, interesting local information about the adequate R1 to R3-groups (site I) and R4-group (site III), to be selected for intensifying binding affinity and activity. Comparison of computed IE for TS CSAMs (Figure 4) classified in three levels of potency (high, moderate, and low) reveals residues the contribution of which to IE is increasable. In the case of CSAMs no relevant substitution suggestion emerged from these this 3 class's analysis. Therefore, a combinatorial design of novel CSAM analogs design through *h*CA II inhibition PH4-based virtual screening of a library of 1,500,625 CSAM analogs.

3.4. 3D-QSAR Pharmacophore Model

3.4.1. *h*CA II Active Site Pharmacophore

The interaction generation protocol in DS program [55] builds protein's active site PH4 features. The larger being the hydrophobic site I accommodating the substrate coumarin heterocycle. The design of CA II inhibitors competitive with the substrate exploits the bottom shrinks of the active site because the active site is conical.

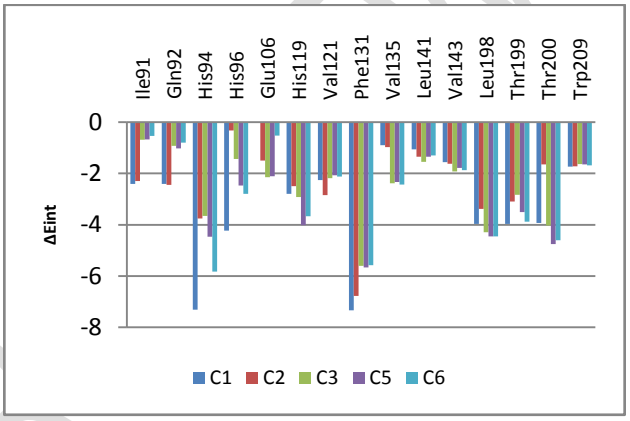

(A)

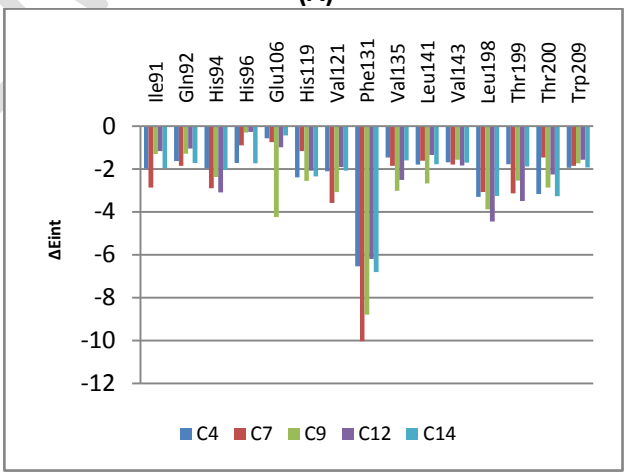

(B)

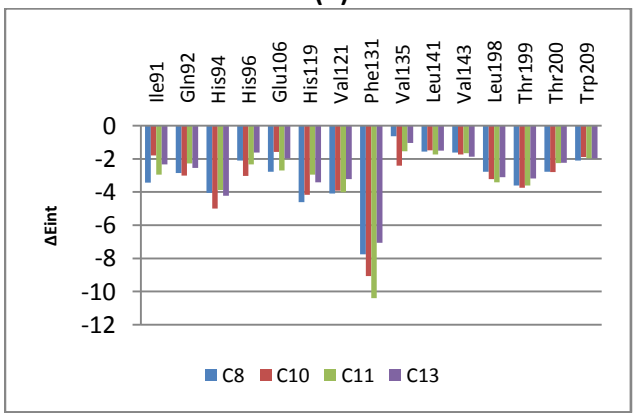

(C)

Figure 4. Molecular mechanics interaction energy E_{int} breakdown to residue contributions in (kcal.mol^{-1}): (A) the most active inhibitors CSAM1,2,3,5 and 6, (B) moderately active inhibitors CSAM4,7,9,12 and 14, (C) less active inhibitors CSAM8,10,11 and 13, Table 2 [32].

3.4.2. Generation and Validation of 3D-QSAR Pharmacophore

The hCA II inhibition 3D-QSAR pharmacophore was generated from the active conformation of 14 CSAM1-14 of the TS and evaluated by 3 compounds CSAM15-17 of the VS covering a moderate range of experimental activities (23 nM – 217 nM). The whole three steps generation process was described earlier [56] resulting in CSAM1 alone as the lead ($IC_{50}^{exp} \leq 2\times23$ nM), none of the training set CSAMx was inactive ($IC_{50}^{exp} > 23\times10^{3.5}$ nM = 72 732 nM) and no starting PH4 features were removed. The top scoring 10 unique PH4 hypotheses were kept, all displaying four-point features. The cost values, correlation coefficients, root-mean square deviation (RMSD) values, the pharmacophore features, and the max-fit value of the top 10 ranked hypotheses (Hypo1 Hypo10) are listed in Table 4. They were selected based on significant statistical parameters, such as high correlation coefficient, low total cost, and low RMSD.

Table 4. Parameters of 10 generated PH4 pharmacophoric hypotheses for CA II inhibitor

Hypothesis	RMSD [a]	R^{2} [b]	Total Costs [c]	Costs Difference [d]	Closest Random [e]
Hypo1	1.207	0.92	48.8	41.3	50.1
Hypo2	1.330	0.90	49.9	40.2	52.6
Hypo3	1.460	0.88	51.5	38.6	53.1
Hypo4	1.495	0.87	52.4	37.7	54.6
Hypo5	1.499	0.87	54.0	36.1	55.9
Hypo6	1.695	0.83	62.5	27.6	63.9
Hypo7	1.999	0.76	64.4	25.7	65.1
Hypo8	2.129	0.72	68.7	21.4	69.0
Hypo9	2.159	0.70	69.8	20.3	71.1
Hypo10	2.161	0.70	70.9	19.2	71.9

[a] root mean square deviation; [b] squared correlation coefficient; [c] overall cost parameter of the PH4 pharmacophore; [d] cost difference between null cost and hypothesis total cost; [e] lowest cost from 49 scrambled runs at a selected level of confidence of 98%. The 98% significance is related to the 49 runs as detailed earlier [42]. The fixed cost = 36.5 with RMSD = 0, the null cost = 90.07 with RMSD = 3.054 and the Configuration cost = 12.84.

The cost parameters of PH4 rang from 48.8 (Hypo1) to 70.9 (Hypo10). The null cost (90.1) is higher than the fixed one (36.5) by Δ = 53.6. A hypothesis near to the fixed cost and far from the null cost as possible is significant from statistical point of view. The interhypotheses RMSD range from 1.207 to 2.161, the squared correlation coefficient (R^2) drops from 0.92 to 0.70. The PH4 hypothesis 1 cost (48.8) closest to the fixed one (36.5) and best RMSD and R^2 was selected for screening. The statistical data (costs, RMSD, R^2) are listed in Table 4 while the configuration cost (12.84 for all hypotheses) is far below 17 as for a reliable pharmacophore.

As described earlier [56], there is 98% chance that pharmacopore hypothesis Hypo1 capacity to predict hCA II inhibition by CSAMx at the same quality level as its parent elaborated complexation QSAR model built from the active ligand conformation and $\Delta\Delta G_{com}$. Another evaluation of Hypo 1 is the mapping of the best active training set CSAM1 (Figure 5) displaying the geometry of the Hypo1 pharmacophore of *h*CA II inhibition. The regression equation for pIC_{50}^{exp} vs. pIC_{50}^{pre} estimated from Hypo1: $pIC_{50}^{exp} = 1.095\times pIC_{50}^{pre} - 0.68$ (n = 14, R^2 = 0.87, R_{xv}^2 = 0.86, F-test = 83.88, σ = 0.02, α > 98 %) is also plotted on Figure 5.

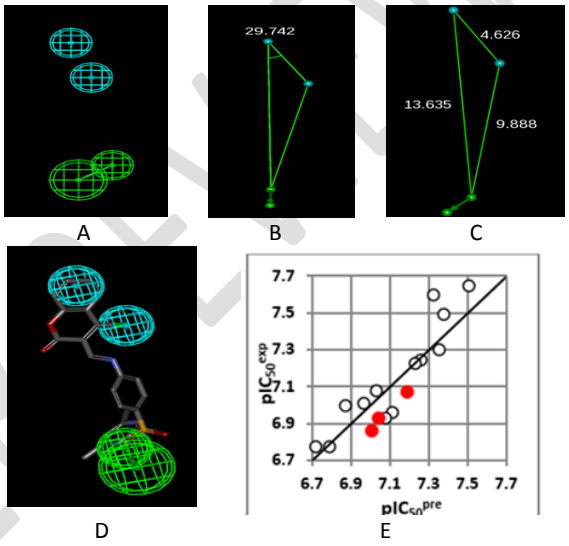

Figure 5. Features: (A) positions of centers, (B) distances between centers of pharmacophoric features, (C) angles between centers, (D) mapping of pharmacophore of hCA II inhibitor with the most potent molecule CSAM1. Feature legend: HYDA = Hydrophobic Aliphatic (turquoase), HBA = Hydrogen bond Acceptor (green). (E) correlation plot of experimental vs. predicted inhibitory activity (blue dots correspond to TS, red dots to VS).

Exploiting the Hypo1 *h*CA II inhibition PH4 hydrophobic features corresponding to R3 substituent at the hydrophobic tail (Scheme 2), novel potent CSAM analogs will be identified from any diverse CSAM library provided they share the same bound conformation as CSAM1-17.

3.5. Virtual library

In silico screening of a VCL is expected to result in hit identification as we reported previously [57, 58]. An initial VCL was enumerated by substitutions at R1 to R4 (see R-groups in Table 5) on the CSAM scaffold. During the process, R-groups numbered from 1 to 35, were attached to R1 to R3 and from 36 to 70 were attached to position R4 resulting in a size of R1 × R2 × R3 × R4 = 35 × 35 × 35 × 35 = 1,500,625 analogs. This initial diversity library was generated from a selection of suitable building blocks (chemicals) listed in the data bases of commercialy available chemicals [59]. Focusing this library to drug-like compounds with a set of

filters and penalties such as the Lipinski rule-of-five (except the restriction $M_w \leq 500$ g/mol) [60] and number of aromatic rings ≤ 5, has reduced the size to 865,670 analogs, 57.68% of its initial population.

3.6. In Silico Screening of Library of CSAMs

Screening of the 865,670 analogs through their mapping to PH4 model Hypo1 resulted in 540 analogs mapping to at least 2 features, 180 to 3. 81 best hits were retained to undergo complexation computations of GFE upon *h*CA II-CSAMx formation to yield their predicted IC_{50}^{pre} determined from equation B (Table 3). They are listed in Table 6.

Table 5: The CSAM scaffold and R-groups (fragments, building blocks, substituents) used in the design of the initial diversity virtual library of CSAM analogues.

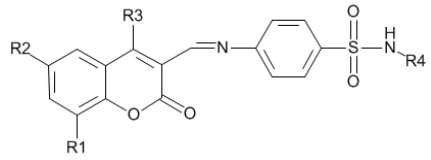

1	2	3	4	5	6	7
----H	----F	----Cl	----Br	----I	----OH	----CH_2F
8	**9**	**10**	**11**	**12**	**13**	**14**
----CH_2Cl	----CH_2Br	----CH_2I	----$C(Me)_3$	----CF_3	----$C(Cl)_3$	----Cl_3
15	**16**	**17**	**18**	**19**	**20**	**21**
----NO_2			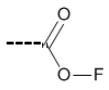	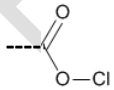	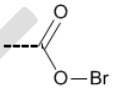	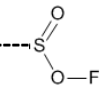
22	**23**	**24**	**25**	**26**	**27**	**28**
		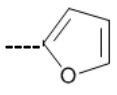	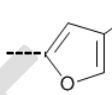	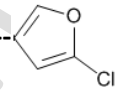	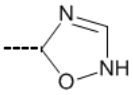	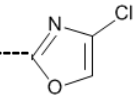
29	**30**	**31**	**32**	**33**	**34**	**35**
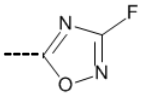	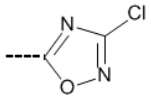	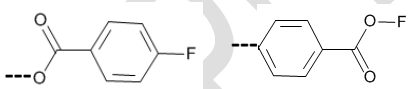		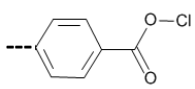	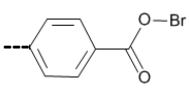	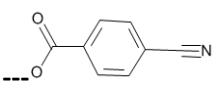

[a] All fragments were used for substitutions in the R_1 and R_2 positions.

Table 6: GFE and their components for the top scoring 81 virtual CSAM analogs. The analog numbering concatenates the index of each substituent R_1 to R_4 with the substituent numbers taken from Table 5.

	Designed Analogs[a]	M_w[b]	$\Delta\Delta H_{MM}$[c]	$\Delta\Delta G_{sol}$[d]	$\Delta\Delta TS_{vib}$[e]	$\Delta\Delta G_{com}$[f]	IC_{50}^{pre}[g]
	CSAM1*		0.0	0.0	0.0	0.0	23[g]
1	2-1-9-23	480	-16.4	1.4	-2.3	-12.7	3.8
2	25-1-9-23	491	-16.4	2.1	7.7	-21.9	1.0
3	1-2-9-23	480	-18.6	-1.6	-2.0	-18.2	1.8
4	23-1-7-23	481	-16.2	-0.8	-2.2	-14.8	2.8
5	5-5-9-23	461	-13.4	-2.2	1.3	-16.9	2.1
6	18-1-9-23	467	-15.0	0.1	-1.2	-13.6	3.3
7	23-1-9-23	451	-11.9	-1.7	0.0	-13.6	3.4
8	28-1-9-23	479	-14.0	-1.5	3.8	-19.3	1.5
9	29-1-9-23	479	-16.9	-1.2	-2.5	-15.7	2.5
10	1-5-9-23	470	-15.8	-3.2	0.7	-19.7	1.4
11	2-5-9-23	472	-14.3	-2.2	0.0	-16.5	2.2
12	22-1-4-23	480	-14.1	-1.9	0.1	-16.1	2.4
13	1-1-9-23	478	-17.7	-0.9	-0.5	-18.1	1.8
14	24-1-9-23	478	-17.8	1.0	0.6	-17.4	2.0
15	23-2-9-23	453	-14.0	0.1	0.0	-13.9	3.2
16	1-1-18-23	462	-17.8	1.5	0.0	-16.2	2.3
17	9-2-18-23	469	-15.3	-0.8	-1.3	-14.8	2.8
18	23-1-7-23	465	-18.0	0.7	-0.4	-16.9	2.1
19	9-22-9-23	441	-11.7	-2.2	3.7	-17.6	1.9
20	29-22-9-23	436	-15.0	0.8	2.1	-16.3	2.3
21	23-19-9-23	476	-13.7	1.8	-0.5	-11.4	4.5
22	18-28-9-23	468	-14.3	-1.3	4.0	-19.6	1.4
23	23-5-9-23	443	-12.2	-1.3	1.5	-14.9	2.8
24	22-10-9-23	494	-16.0	0.2	-0.1	-15.7	2.5
25	22-10-9-23	466	-14.3	0.3	-0.5	-13.5	3.4
26	9-9-9-23	489	-15.0	-2.3	-2.0	-15.3	2.6
27	30-22-9-23	460	-15.1	-1.1	2.3	-18.6	1.7
28	23-29-9-23	452	-13.7	-2.1	-0.6	-15.2	2.7
29	28-5-4-23	515	-14.6	-1.3	1.2	-17.0	2.1
30	1-29-9-23	479	-18.1	-1.1	-2.3	-16.9	2.1
31	11-22-9-23	495	-15.0	-2.7	0.5	-18.2	1.8
32	19-23-9-23	494	-15.8	-0.8	-1.1	-15.6	2.5
33	22-23-9-23	408	-11.4	-1.7	2.9	-16.1	2.4
34	9-25-9-23	497	-14.6	-2.2	9.9	-26.7	0.5
35	13-30-9-23	478	-14.1	0.7	0.3	-13.8	3.3
36	22-30-9-23	460	-13.3	0.5	1.6	-14.3	3.0

Designed Analogs[a]	M_w[b]	$\Delta\Delta H_{MM}$[c]	$\Delta\Delta G_{sol}$[d]	$\Delta\Delta TS_{vib}$[e]	$\Delta\Delta G_{com}$[f]	IC_{50}^{pre}[g]
37	22-28-9-23	436	-12.4	-3.5	2.4	-18.2	1.7
38	22-11-9-23	495	-15.0	0.0	-0.5	-14.6	2.9
39	22-18-9-23	424	-12.4	-2.0	1.9	-16.3	2.3
40	9-18-29-23	468	-16.8	-0.9	-1.8	-15.9	2.4
41	24-29-9-23	445	-18.8	1.8	-0.7	-16.3	2.3
42	13-5-9-23	454	-13.0	-1.8	1.7	-16.5	2.2
43	23-23-7-23	481	-16.4	2.3	1.2	-15.3	2.6
44	22-28-4-23	497	-12.2	1.0	1.5	-12.8	3.7
45	28-23-4-23	453	-12.3	2.0	2.9	-13.2	3.6
46	24-18-9-23	467	-15.9	0.2	-0.1	-15.6	2.5
47	13-24-9-24	479	-11.3	0.1	-2.0	-9.3	6.1
48	5-25-18-24	493	-12.5	-2.0	7.5	-22.0	1.0
49	18-28-9-24	495	-10.8	-0.9	4.3	-16.0	2.4
50	18-24-9-24	493	-12.6	0.2	0.3	-12.7	3.7
51	5-28-9-24	497	-10.6	-1.2	1.3	-13.1	3.6
52	22-24-7-24	491	-12.6	0.8	-2.5	-9.3	6.1
53	18-24-18-24	477	-10.5	-1.2	1.0	-12.8	3.7
54	18-22-18-10	493	-8.6	-5.7	-1.5	-12.8	3.7
55	23-22-9-10	494	-6.4	-3.7	-2.8	-7.4	8.0
56	22-22-5-10	464	-6.4	-4.1	-1.5	-9.0	6.3
57	18-22-18-11	494	-3.7	-4.0	-3.0	-4.7	11.6
58	5-23-18-21	476	-8.8	-3.4	-2.4	-9.8	5.7
59	9-22-9-23	441	-11.7	-0.6	3.7	-15.9	2.4
60	23-22-18-20	458	-13.2	3.4	-0.5	-9.3	6.1
61	18-23-18-20	490	-15.3	3.8	-3.1	-8.4	7.0
62	22-9-18-20	490	-15.9	2.1	-2.0	-11.7	4.4
63	13-18-18-20	492	-16.2	2.4	-2.8	-10.9	4.9
64	18-13-18-19	496	-15.7	-5.0	-2.8	-17.9	1.8
65	28-22-5-20	488	-13.9	3.4	-0.8	-9.8	5.7
66	28-22-18-19	490	-15.3	-4.4	1.8	-21.5	1.1
67	22-24-5-21	484	-10.2	-3.3	-1.9	-11.5	4.5
68	24-22-18-20	484	-14.4	4.6	-1.9	-7.9	7.4
69	28-22-9-31	519	-13.1	2.7	0.8	-11.2	4.7
70	24-23-5-31	519	-15.7	4.3	-4.6	-6.8	8.6
71	22-24-9-24	476	-7.5	0.4	-0.5	-6.6	9.0
72	18-25-18-23	464	-15.2	-1.9	10.3	-27.3	0.5
73	18-25-9-23	480	-15.1	-2.0	10.0	-27.1	0.5
74	9-25-18-23	480	-14.7	-1.9	9.8	-26.4	0.6
75	18-25-4-23	525	-15.1	-1.6	9.5	-26.1	0.6
76	18-25-18-29	492	-17.8	-1.4	10.7	-29.9	0.3
77	18-25-9-29	508	-17.9	-1.7	11.3	-30.9	0.3
78	9-25-9-29	525	-17.3	-2.0	9.8	-29.1	0.4
79	9-25-9-10	582	-8.1	-5.2	3.3	-16.5	2.2
80	18-25-9-31	563	-14.1	-2.8	7.0	-23.8	0.8
81	4-25-9-29	569	-17.0	-1.6	9.7	-28.4	0.4

For table foot notes see Table 2.

3.7. Novel CSAM analogs

To enumerate the VCL of novel CSAMs, we take account of E-I interactions and its related geometrical information to select suitable substituents (R1- to R4-groups). In this regard the R-groups occurrence in the 81 best hits identified by the PH4 is an interesting criterion. Figure 6 displays the histograms for each R1- to R4- groups represented in the CSAMs subset. We can see that the highest occurrence at R1 position is observed for 9(50-times) and 18(16-times) while at R2 position 22(13-times) and 25(12-times). Concerning R3 groups, the highest frequency of occurrence in the CSAMs subset dispalyed 18(15-times), 22(14-times), 23(10-times) and 9(8-times). The R4 groups include chiefly fragments 55(6-times), 58(51-times) and 59(8-times). The top six scoring virtual hits, namely, are analogs: 18-25-9-29 (IC_{50}^{pre}=0.3nM), 18-25-18-29 (IC_{50}^{pre}=0.3 nM), 9-25-9-29 (IC_{50}^{pre}=0.4 nM), 4-25-9-29 (IC_{50}^{pre} =0.4 nM), 18-25-18-23 (IC_{50}^{pre}=0.5 nM), 18-25-9-23 (IC_{50}^{pre}=0.5 nM). The substitutions on the coumarin ring and sulfonamide moiety of CSAMs led to higher IC_{50}^{pre} of the novel analogs. The IC_{50}^{pre} of 18-25-9-29 reached a value of 0.3 nM, approximately 80 times the most active TS CSAM1's potency (IC_{50}^{exp} = 23 nM), Figures 7 and 8.

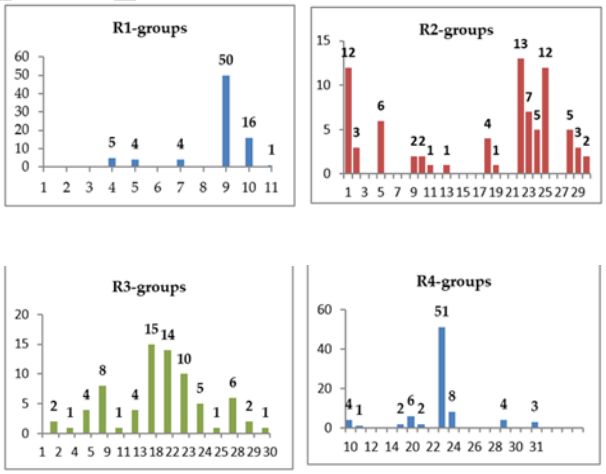

Figure 6. Histograms of frequency of occurrence of individual R_1–R_4 groups in the 81 selected analogues mapping to the feature pharmacophore hypothesis Hypo1 (for fragments numbering see Table 5)

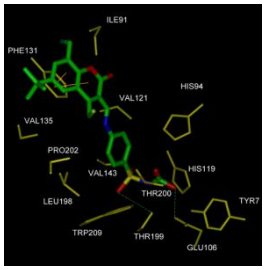

(A)

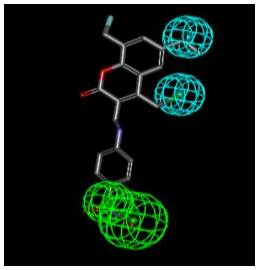

(B)

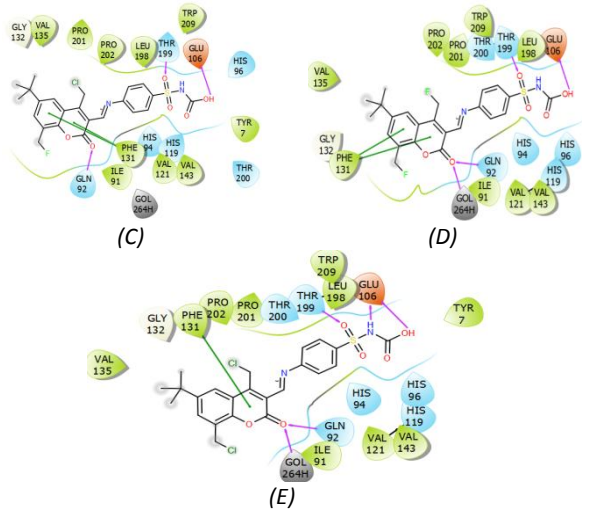

Figure 7. (A) Close up of virtual hit CSAM18-25-9-29, the most active designed CSAM analog (IC_{50}^{pre} = 0.3 nM) at the active site of hCA II. Interacting residues are colored yellow, and NADH is not shown for clarity. (B) Mapping of the CSAM 18-25-9-29 to hCA II inhibition pharmacophore. (C) 2D schematic interaction diagram of the CSAM 18-25-9-29 at the active site of hCA II. (D) 2D schematic interaction diagram of the analog CSAM 18-25-18-29 (IC_{50}^{pre} = 0.3 nM) at the active site of hCA II. (E) 2D schematic interaction diagram of the analog CSAM 9-25-9-29 (IC_{50}^{pre} = 0.4 nM) at the active site of hCA II.

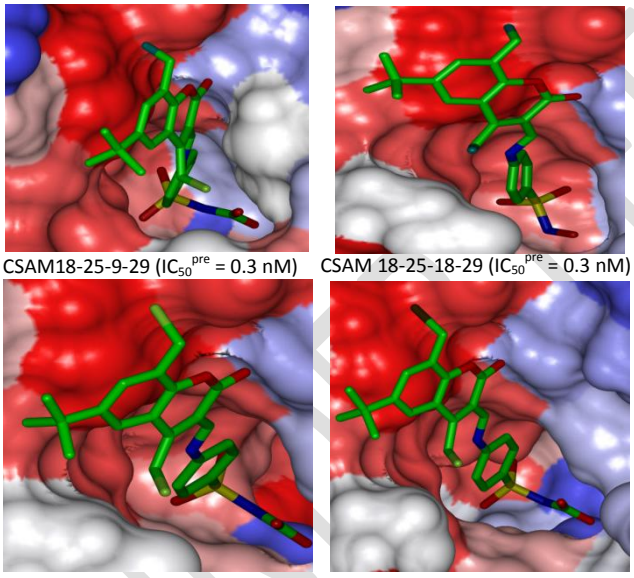

CSAM18-25-9-29 (IC_{50}^{pre} = 0.3 nM) CSAM 18-25-18-29 (IC_{50}^{pre} = 0.3 nM)

CSAM 9-25-9-29 (IC_{50}^{pre} = 0.4 nM) CSAM 4-25-9-29 (IC_{50}^{pre} = 0.42 nM)

Figure 8. Molecular surface of the active site of *h*CA II with bound 4 best active designed CSAM analogs. For surface coloring legend see Figure 3.

3.8. Pharmacokinetic profile of novel CSAM analogs

The pharmacokinetic profile of the *h*CA II inhibitors remains an important issue. The best-studied drug to treat glaucoma is acetazolamide (AAZ), which is frequently administered in long-term treatments owing to its efficient reduction of IOP and high affinity towards *h*CA II, minimal toxicity, and very low oral bioavailability due to its poor human oral absorption (HOA) [44]. The descriptors, their range for 95% of known drugs were described earlier [54]. In line with the observed unfavorable pharmacokinetic exposure for the best active AAZ, the predicted oral bioavailability of novel CSAM analogs ranges from 56% to 87%. Since a value greater than 56% is considered good, 7 analogs among the best predicted 27 CSAMs display HOA greater than 80%. Drug likeness (#stars), the global ADME-related compound selection criterion values at 0 violation for the best active designed CSAMs are better than AAZ with 2 violations. Thus the best designed CSAMs display favorable pharmacokinetic profiles.

Table 7. ADME-related properties of the best designed CSAM analogs and known antiglaucoma agents either in clinical use or currently undergoing clinical testing computed by QikProp [33].

Analogs[a]	#stars[b]	M_W[c] (g.mol^{-1})	S_{mol}[d] (Å^2)	S_{m+hfo}[e] (Å^2)	V_{mol}[f] (Å^3)	rotB[g]	HB_{don}[h]	HB_{acc}[i]	$logP_{o/w}$[j]	$logS_{wat}$[k]	BIP_{caco}[l] (nm.s^{-1})	logB/B[m]	#meta[n]	$logK_{hsa}$[o]	IC_{50}^{pre}[p] [nM]	HOA[q]	%HOA[r]
5-5-9-23	2	461	680.2	37.3	1182	6	2	8.0	2.7	-5.7	71.1	-1.7	1	0.1	2.1	3	76
9-22-9-23	1	441	688.9	91.7	1194	6	2	8.0	2.6	-5.5	78.4	-1.8	2	0.1	1.9	3	76
23-5-9-23	1	443	666.2	37.0	1158	7	3	8.8	1.5	-4.7	23.1	-2.4	2	-0.2	2.8	2	60
22-10-9-23	1	494	740.8	36.4	1300	6	2	10.0	2.3	-5.7	44.8	-2.2	2	-0.1	2.5	2	70
9-9-9-23	3	489	737.1	133.8	1297	6	2	8.0	3.3	-6.6	73.4	-1.8	3	0.3	2.6	1	80
11-22-9-23	1	495	735.9	36.1	1288	6	2	11.0	1.6	-5.3	0.2	-2.6	1	-0.3	1.8	2	60
22-23-9-23	1	408	641.0	37.2	1111	7	3	8.8	1.0	-4.1	21.6	-2.5	2	-0.3	2.4	2	57

9-25-9-23	2	497	797.7	288.1	1421	7	2	8.0	3.8	-7.1	74.6	-2.1	2	0.6	0.5	1	83
22-11-9-23	1	495	735.3	36.5	1286.7	6	2	11.0	1.5	-5.3	16.5	-2.6	1	-0.3	2.9	2	57
22-18-9-23	1	424	666.7	89.1	1161.2	6	2	8.0	2.2	-5.0	70.4	-1.9	2	0.1	2.3	3	73
18-22-18-10	1	493	762.5	91.6	1337.2	6	1	10.0	3.2	-6.1	216.6	-1.3	3	0.1	3.7	3	88
23-22-9-10	1	494	747.9	33.4	1310.4	7	2	10.8	2.2	-5.4	64.3	-2.1	3	-0.2	8.0	3	73
22-22-5-10	1	464	711.4	6.5	1236.8	6	1	10.0	2.5	-5.0	196.1	-1.4	1	-0.3	6.3	3	83
18-22-18-11	2	494	765.4	88.6	1333.6	6	1	11.0	2.4	-5.7	69.6	-1.9	2	-0.3	11.6	2	74
5-23-18-21	1	476	740.1	39.0	1296.7	7	2	9.3	2.9	-5.7	114.2	-1.8	3	0.1	5.7	3	81
9-22-9-23	1	441	689.6	86.6	1196.7	6	2	8.0	2.6	-5.5	72.4	-1.9	2	0.1	2.4	3	75
18-13-18-19	2	496	753.5	89.8	1315.3	6	1	11.0	2.3	-5.6	66.2	-1.9	2	-0.3	1.8	2	73
18-25-18-23	1	464	755.5	281.1	1351.5	7	2	8.0	3.2	-6.2	72.7	-2.1	2	0.4	0.5	1	79
18-25-9-23	2	480	765.8	272.7	1374.6	7	2	8.0	3.4	-6.5	72.6	-2.1	2	0.4	0.5	1	80
9-25-18-23	2	480	767.8	274.9	1377.9	7	2	8.0	3.5	-6.5	73.0	-2.1	2	0.5	0.6	1	81
18-25-4-23	1	525	769.4	271.5	1382.3	8	2	8.0	3.5	-6.4	72.4	-2.1	2	0.4	0.6	1	68
18-25-18-29	2	492	770.3	275.6	1403.3	6	1	7.5	4.1	-6.8	9.3	-2.3	2	0.5	0.3	1	69
18-25-9-29	2	508	779.8	267.1	1425.7	6	1	7.5	4.4	-7.1	9.3	-2.3	2	0.6	0.3	1	60
9-25-9-29	2	525	791.9	261.5	1452.6	6	1	7.5	4.6	-7.4	9.5	-2.3	2	0.6	0.4	1	59
9-25-9-10	5	582	882.5	261.8	1597.7	7	1	10.0	4.8	-8.1	160.7	-1.6	3	0.6	2.2	1	81
4-25-9-29	2	569	796.2	260.6	1460.8	7	1	7.5	4.7	-7.3	9.3	-2.3	2	0.6	0.4	1	59
SA	0	172	354	0	547	3	3	5.0	-1	-1	111	-1	1	-1	260	2	59
AAZ	2	222	409	104	639	4	2	7.0	-1	-1	32	-2	1	-1	16	2	46
HMN-214	0	379	673	155	1197	7	0	6.0	4	-4	1586	-1	4	0	---	3	100
E-7071	0	371	636	94	1105	7	3	7.0	2	-4	342	-1	5	0	---	3	85
E-7070	1	386	585	0	1010	5	4	9.0	1	-3	57	-2	1	0	---	3	62
T138067	2	371	528	89	905	4	1	5.0	3	-4	1634	0	1	0	---	3	100

[a] designed CSAM analogues, Table 7; [b] drug-likeness; [c] molecular weight in g mol^{-1}; [d] total solvent-accessible molecular surface, in $Å^2$; [e] hydrophobic (hfo) portion of the solvent-accessible molecular surface, in $Å^2$; [f] total volume of molecule enclosed by solvent-accessible molecular surface, in $Å^3$; [g] number of non-trivial (not CX_3), non-hindered rotatable bonds; [h] estimated number of hydrogen bonds donors; [i] estimated number of hydrogen bonds acceptors; [j] logarithm of partitioning coefficient between n-octanol and water (o/w) phases; [k] logarithm of predicted aqueous solubility; [l] logarithm of predicted binding constant to human serum albumin; [m] logarithm of predicted brain/blood partition coefficient; [n] predicted apparent Caco-2 cell membrane permeability in Boehringer-Ingelheim scale, in nm/s; [o] number of likely metabolic reactions; [p] predicted half-maximal inhibitory concentrations IC_{50}^{pre}; [q] human oral absorption; [r] percentage of human oral absorption in gastrointestinal tract; * star indicating that the property descriptor value falls outside the range of values for 95% of known drugs.

3.9. Discussions

To date, the most exhaustive and recent review about the multiple binding modes of *h*CA II inhibitors reported by Supuran reveals four binding modes and inhibition mechanisms: (i) coordination to the catalytic metal ion to prevent the zinc binding for the substrate; (ii) anchoring to the zinc-coordinated water; (iii) occlusion of the active site entrance and (iv) binding outside the active site [61]. Coumarin sulfonamides bind to *h*CA II through the mechanism III in line with the moderate size of the R4 substituent.

The most comprehensive study on *h*CA II inhibition has been reported by Temperini *et al.* who, in order to understand the inhibitory mechanism of *h*CA II, resolved the X-ray crystal structure (at a resolution of 2.0 Å) of a drug forming adduct with the physiologically dominant CA isoform, *h*CA II [53]. They observed hydrogen bonds and hydrophobic van der Waals interactions with several amino acid residues, such as Phe131 with both cycles and heterocycles of the coumarin and stacking with the residue Phe131 as well as interactions involving Leu198, Gln92, Thr199, Thr200, His94, His96, His119, Glu106, known from previous X-ray crystallographic works to interact with other classes of inhibitors (sulfonamides, sulfamates, coumarins), (PDB codes: 3F8E, 3HS4, 3ML2 and 3IEO) [34, 53, 62, 63]. According to our analysis of the *h*CA II - CSAMx complexes of most potent inhibitors, some of these interactions play a key role in the significant improvement of predicted inhibitory potencies of the proposed novel sulfonamides. Figure 9 displays noticeable contributions of Phe131, Ile91, Gln92, Thr199 to the E_{int} of CSAMs to *h*CA II active site. These are almost the same for all of the best analogs of CSAM which underlines the impact of these interactions to increased *h*CA II inhibition. This can be observed also in the Figure 4, where the most active ligand CSAM1 of the TS [32] shows strong interactions with these amino acid residues. As displayed in Figure 10, we show an improvement of interaction energy E_{int} with Glu106 that seems to be one of the key determinants for binding affinity for the *h*CA II inhibitors. Previous results clearly show that the hydrogen bond of this amino acid residue is functionally important for efficient catalysis of CO_2 hydration or ester hydrolysis [64, 65]. This structural specificity that emerged during the PH4 screening of the virtual library of sulfonamide analogs led to identification of new hits, the best of which are capable of increasing

the E_{int} with the Glu106 and Thr200 residues while maintaining strong interactions with the other active site residues cited above.

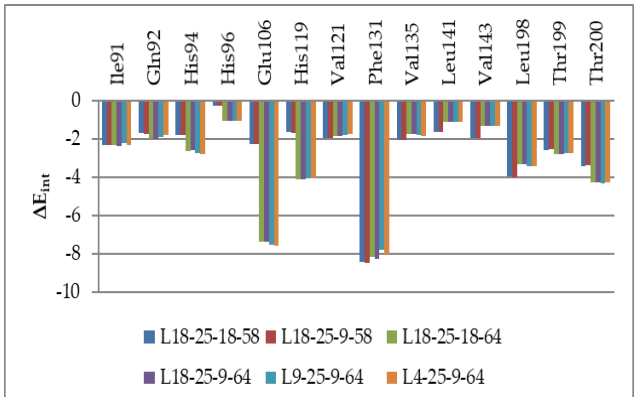

Figure 9: Molecular mechanics inhibitor-active site residues interaction energy E_{int} (Table 1) for best five designed novel CSAM analogs (the color coding refers to ligands given in the legend).

Conclusions

Novel *h*CA II direct inhibitors containing the coumarin moiety reaching low nanomolar range of the predicted IC_{50}^{pre} (Table 6, Figure 8). Despite they are somewhat too optimistic, they suggest that the coumarin-type *h*CA II inhibitors displaying higher potency compared with the reported CSAMs [18] may exist. Our QSAR model has utilized the bound CSAM active conformation, to reach structural determinants from E_{int} breakdown to active site residue contribution necessary to improve the binding and the number of favorable contacts of the three *h*CA II active site subsites (I, II, and III). The derived 3D QSAR pharmacophore identified during the chemical space exploration around the R1 to R4 positions novel CSAMs analogs with predicted nanomolar *h*CA II inhibitory potencies 18-25-9-29 (IC_{50}^{pre} = 0.3 nM), 18-25-18-29 (IC_{50}^{pre} = 0.3 nM), 9-25-9-29 (IC_{50}^{pre} = 0.4 nM), 4-25-9-29 (IC_{50}^{pre} = 0.4 nM), 18-25-18-23 (IC_{50}^{pre} = 0.5 nM), 18-25-9-23 (IC_{50}^{pre} = 0.5 nM). All of these new CSAMs display favorable pharmacokinetic profiles compared to current antiglaucoma therapeutics. We believe that these compounds are worth synthesizing and experimental testing for the *h*CA II inhibitory potency.

References

1 Tham, Y.C.; Li, X.; Wong, T.Y.; Quigley, H.A.; Aung, T.; Cheng, C.Y. Global prevalence of glaucoma and projections of glaucoma burden through 2040: a systematic review and meta-analysis. Ophthalmology, **2014**; 121, 2081–2090. DOI : 10.1016/j.ophtha.2014.05.013

2 WHO: "World Report on Vision", https://www.who.int/ publications-detail/world-report- on-vision ISBN: 978-92-4-151657-0, October **2019**: 25

3 Jonas, J.B. ; Aung, T.; Bourne, R.R.; Bron, A.M.; Ritch, R.; Panda-Jonas, S. Glaucoma. *Lancet*, **2017**, 390, 2183–2193. DOI : 10.1016/S0140-6736(17)31469-1.

4 Mehran, N.A.; Sinha, S.; Razeghinejad, R. New glaucoma medications: latanoprostene bunod, netarsudil, and fixed combination netarsudil-latanoprost. Eye, **2020**, 34, 72–88. DOI: 10.1038/s41433-019-0671-0.

5 Harwerth, R.S.; Carter-Dawson, L.; Shen, F.; Smith 3rd, E.L.; Crawford, M.L. Ganglion cell losses underlying visual field defects from experimental glaucoma. Invest Ophthalmol. Vis. Sci. **1999**, 40, 2242–2250.

6 Harwerth, R.S.; Carter-Dawson, L.; Smith 3rd, E.L.; Barnes G.; Holt, W.F., Crawford, M.L.J. Neural losses correlated with visual losses in clinical perimetry. Invest. Ophthalmol. Vis. Sci. **2004**, 45, 3152–3160. DOI : 10.1167/iovs.04-0227

7 Mayro, E.L.; Wang, M.; Elze, T.; Pasquale, L.R. The impact of artificial intelligence in the diagnosis and management of glaucoma. Eye, **2020**, 34, 1–11. DOI : 10.1038/s41433-019-0577-x

8 Supuran, C.T.; Scozzafava, A. Bioorganic and Medicinal Chemistry **2007**, 15, 4336-4350. DOI: 10.1016/j.bmc.2007.04.020

9 Krishnamurthy, V.M.; Kaufman, G.K.; Urbach, A.R.; Gitlin, I.; Gudiksen, K.L.; Weibel, D.B.; Whitesides, G.M. Carbonic anhydrase as a model for biophysical and physical-organic studies of proteins and protein-ligand binding. Chem. Rev. **2008**, 108, 946-1051. DOI: 10.1021/cr050262p

10 Rummer, J.L.; McKenzie, D.J.; Innocenti, A.; Supuran, C.T.; Brauner, C.J. Root effect hemoglobin may have evolved to enhance general tissue oxygen delivery. *Science*. **2013**, 340, 1327-1329. DOI: 10.1126/science.1233692

11 Supuran, C.T. Diuretics: From classical carbonic anhydrase inhibitors to novel applications of the sulfonamides. *Curr. Pharm. Des.* **2008**, 14, 641–648. DOI: 10.2174/138161208783877947

12 Supuran, C. T.; Di Fiore, A.; De Simone, G. Carbonic anhydrase inhibitors as emerging drugs for the treatment of obesity. *Expert Opin. Emerging Drugs*. **2008**, 13, 383–392. DOI : 10.1517/14728214.13.2.383

13 De Simone, G.; Di Fiore, A.; Supuran, C. T. Are carbonic anhydrase inhibitors suitable for obtaining antiobesity drugs? *Curr. Pharm. Des.* **2008**, 14, 655–660. DOI: 10.2174/138161208783877820

14 Thiry, A.; Dogné, J.M.; Masereel, B.; Supuran, C.T. Targeting tumor-associated carbonic anhydrase IX in cancer therapy. *Trends Pharmacol. Sci*. **2006**, 27, 566–573. DOI: 10.1016/j.tips.2006.09.002

15 Winum, J. Y.; Rami, M.; Scozzafava, A.; Montero, J. L.; Supuran, C. Carbonic Anhydrase IX: a new druggable target for the design of antitumor agents. *Med. Res. Rev*. **2008**, 28, 445–463. DOI: 10.1002/med.20112

16 Supuran, C. T.; Scozzafava, A.; Casini, A. Carbonic anhydrase inhibitors. *Med. Res. Rev.* **2003**, 23, 146–189. DOI: 10.1002/med.10025

17 Liljas, A.; Kannan, K.K.; Bergsten, P.C.; Waara, I.; Fridborg, K.; Strandberg, B.; Carlbom, U.; Järup, L.; Lövgren, S.; Petef, M. Crystal structure of human carbonic anhydrase C. *Nature, New Biol.* **1972**, 235, 131-137.

18 Svastova, E.; Hulíkova, A.; Rafajova, M.; Zatovicova, M.; Gibadulinova, A.; Casini, A.; Cecchi, A.; Scozzafava, A.; Supuran, C. T.; Pastorek, J.; Pastorekova, S. Hypoxia activates the capacity of tumor-associated carbonic anhydrase IX to acidify extracellular pH. *FEBS Lett.* **2004**, 577, 439–445. DOI: 10.1016/j.febslet.2004.10.043

19 Ghorai, S.; Pulya, S.; Ghosh, K.; Panda, P.; Ghosh, B.; Gayen, S. Structure-activity relationship of human carbonic anhydrase-II inhibitors: Detailed insight for future development as anti-glaucoma agents, *Bioorganic Chemistry*, **2020,** 95, 103557. https://doi.org/10.1016/j.bioorg.2019.103557.

20 Ibrahim, S. S.; Salem, M.M.; Abd Elsalam, H.A.; Noser, A.A. Design, synthesis, in-silico and biological evaluation of novel 2-Amino-1,3,4-thiadiazole based hydrides as B-cell lymphoma-2 inhibitors with potential anticancer effects, *Journal of Molecular Structure*, **2022**, 1268, 133673. https://doi.org/10.1016/j.molstruc.2022.133673.

21 Anitha, D.; Suganthi, M.;· Gnanendra, S.; Govarthanan, M. Identification of Potential Carbonic Anhydrase Inhibitors for Glaucoma Treatment Through an *In Silico* Approach, *Int. J. Pept. Res. Therapeut*. **2020**, 26, 2147–2154. https://doi.org/10.1007/s10989-019-10011-8

22 Supuran, C.T. An update on drug interaction considerations in the therapeutic use of carbonic anhydrase inhibitors, *Expert Opin Drug Metab Toxicol*. **2020**, 16, 297-307. https://doi.org/10.1080/17425255.2020.1743679

23 Jansook, P.; Hnin, H. M.; Loftsson, T.; Stefánsson, E. Cyclodextrin-based formulation of carbonic anhydrase inhibitors for ocular delivery – A review, *International Journal of Pharmaceutics,* **2021**, 606, 120955. https://doi.org/10.1016/j.ijpharm.2021.120955.

24 Hollo, G. ; Chiselita, D. ; Petkova, N. ; Cvenkel, B. ; Liehneova, I. ; Izgi, B. ; Berta, A. ; Szaflik, J. ; Turacli, E. ; Stewart, W.C. The efficacy and safety of timolol maleate versus brinzolamide each given twice daily added to travoprost in patients with ocular hypertension or primary open-angle glaucoma. *Eur. J. Ophthalmol*. **2006**, 16, 816–823. DOI : 10.1177/112067210601600606

25 Dutt VA, Patel A, Cholkar K, Mitra AK. Recent patents on emerging therapeutics for the treatment of glaucoma, age related macular degeneration and uveitis. *Curr. Biomed. Eng*. **2012**, 5, 83–101. DOI : 10.2174/18747 64711205010083

26 Nguyen, Q.H. Combination of brinzolamide and brimonidine for glaucoma and ocular hypertension: critical appraisal and patient focus. *Patient Prefer. Adherence*, **2014,** 8, 853–864. DOI : 10.2147/PPA.S53162

27 Lusthaus, J.A.; Goldberg, I. Brimonidine and brinzolamide for treating glaucoma and ocular hypertension; a safety evaluation. *Expert Opin. Drug Safety*, **2017**, http://dx.doi.org/10.1080/14740338.2017.1346083

28 Hou, Z.; Li, C.; Liu Y.; Zhang, M.; Wang, Y.; Fan, Z.; Guo, C.; Lin, B. and Liu, Y. Design, synthesis and biological evaluation of carbohydrate-based sulphonamide derivatives as topical antiglaucoma agents through selective inhibition of carbonic anhydrase II, *J. Enz. Inhib. Med. Chem*., **2020**, 35, 383–390, DOI : 10.1080/ 14756366.2019.1705293

29 Ghorai, S. ; Pulya, S. ; Ghosh, K. ; Panda, P. ; Ghosh, B. ; Gayen, S. Structure-activity relationship of Human Carbonic Anhydrase-II inhibitors: Detailed Insight for future development as antiglaucoma agents, *Bioorg. Chem.*, **2020**, 95:103557. DOI : 10.1016/j.bioorg.2019. 103557.

30 Maresca, A. ; Temperini, C. ; Vu, H. ; Pham, N. B. ; Poulsen, S.A. ; Scozzafava, A. ; Quinn, R.J. ; Supuran, C.T. Non-Zinc Mediated Inhibition of Carbonic Anhydrases: Coumarins Are a New Class of Suicide Inhibitors. *J. Am. Chem. Soc.* **2009**, 131, 3057–3062. DOI : 10.1021/ ja809683v

31 Wang, Z.C. ; Duan, Y.T. ; Qin, Y.J. ; Wang, P.F. ; Luo, Y. ; Wen, Q. ; Yang, Y.A. ; Sun ,J. ; Hu, Y. ; Sang, Y.L. ; Zhu, H.L. Potentiating 1-(2-hydroxypropyl)-2-styryl-5-nitroimida-zole derivatives against antibacterial agents: design, synthesis and biology analysis. *Eur. J. Med. Chem.*, **2013**, 65, 456-463. DOI: 10.1016/j.ejmech.2013.05.004

32 Wagner, J.; Avvaru, B.S.; Robbins, H.A.; Scozzafava, A.; Supuran, C.T.; McKenna, R. Coumarinyl-substituted sulfonamides strongly inhibit several human carbonic anhydrase isoforms: solution and crystallographic investigations. Bioorg. Med. Chem. **2010**, 18, 4873–4878. DOI : 10.1016/j.bmc.2010.06.028

33 QikProp, version 3.7, release 14, X Schrödinger, LLC, New York, NY, **2014**.

34 Sippel, K.H.; Robbins, A.H.; Domsic, J.; Genis, C.; Agbandje-McKenna, M.; McKenna, R. High-resolution structure of human carbonic anhydrase II complexed with acetazolamide reveals insights into inhibitor drug design. *Acta Crystallogr Sect F Struct Biol Cryst Commun.* **2009**, 65, 992-995. DOI: 10.1107/S1744309109036665.

35 Insight-II and Discover molecular modeling and simulation package, Version 2005. San Diego, CA: *Accelrys*, Inc. **2005**.

36 (a) Kouassi, A.F.; Kone, M.; Keita, M.; Esmel, A.; Megnassan, E.; N'Guessan, Y.T.; Frecer, V.; Miertus, S. Computer-aided design of orally bioavailable pyrrolidine carboxamide inhibitors of Enoyl-Acyl Carrier Protein Reductase of Mycobacterium tuberculosis with favorable pharmacokinetic profiles. *Int. J. Mol. Sci.* **2015**, 16, 29744–29771. https://doi.org/10.3390/ijms161226196. (b) Kouman KC, Keita M, Kre N'Guessan R, et al. Structure-Based Design and in Silico Screening of Virtual Combinatorial Library of Benzamides Inhibiting 2-trans Enoyl-Acyl Carrier Protein Reductase of Mycobacterium tuberculosis with Favorable Predicted Pharmacokinetic Profiles. *Int. J. Mol. Sci.* 2019; **20**(19): 4730.

37 Gilson, M.K.; Honig, B. The inclusion of electrostatic hydration energies in molecular mechanics calculations. *J. Comput. Aid Mol. Des.* **1991**, 5, 5–20.

38 Allangba, K.N.P.G.; Keita, M.; Kre N'Guessan, R.; Megnassan, E.; Frecer, V.; Miertus, S. Virtual design of novel Plasmodium falciparum cysteine protease falcipain-2 hybrid lactone-chalcone and isatin-chalcone inhibitors probing the S2 active site pocket. *J. Enz. Inhib. Med. Chem.* **2018**, 34, 547–561. DOI : 10.1080/ 14756366.2018.1564288

39 Frecer, V.; Miertus, S.; Tossi, A.; Romeo, D. Rational design of inhibitors for drug-resistant HIV-1 aspartic protease mutants. *Drug Des. Discov.* **1998**, 15, 211–231.

40 Dali, B.; Keita, M.; Megnassan, E.; Frecer, V.; Miertus, S. Insight into selectivity of peptidomimetic inhibitors with modified statine core for plasmepsin II of *Plasmodium falciparum* over human Cathepsin D. *Chem. Biol. Drug Des.* **2012**, 79, 411–430. DOI: 10.1111/j.1747-0285. 2011.01276.x

41 Megnassan, E.; Keita, M.; Bieri, C.; Esmel, A.; Frecer, V.; Miertus, S. Design of novel dihydroxynaphthoic acid inhibitors of *Plasmodium Falciparum* Lactate Dehydrogenase. *Med. Chem.* **2012**, 8, 970–984. DOI : 10.2174/157340612802084324

42 Esmel, A.; Keita, M.; Megnassan, E.; Beguemsi, T.; Frecer, V.; Miertus, S. Insight into binding mode of nitrile inhibitors of Plasmodium falciparum falcipain-3, QSAR and pharmacophore models, virtual design of new analogues with favorable pharmacokinetic profiles. *SDRP J. Comput. Chem. Mol. Model.* **2017**, 2, 103–124. DOI: 10.25177/JCMP.2.1.5

43 Owono, L.C.; Keita, M.; Megnassan, E.; Frecer, V.; Miertus, S. design of thymidine analogs targeting thymidilate kinase of *Mycobacterium tuberculosis*. *Tuberculosis Res. Treat.* **2013**, 1-13, ID 670836 (2013). http://dx.doi.org/10.1155/2013/670836.

44 Frecer, V.; Megnassan, E.; Miertus, S. Design and *in silico* screening of combinatorial library of antimalarial analogs of triclosan inhibiting *Plasmodium falciparum* enoyl-acyl carrier protein reductase. *Eur. J. Med. Chem.* **2009**, 44, 3009–3019. DOI: 10.1016/j.ejmech.2008.12.028.

45 De-Eknamkul, W.; Umehara, K.; Monthakantirat, O.; Toth, R.; Frecer, V.; K.; Knapich, L.; Braiuca, P.; Hiroshi, N.; Miertus, S. QSAR study of natural estrogen-like isoflavonoids and diphenolics from Thaï medicinal plants. *J. Mol. Graph. Model.* **2011**, 29, 784-794. DOI: 10.1016/j.jmgm.2011.01.001.

46 Sapse, A.M., Schwiezer, B. S., Dicker, A. P., Bertino, J. R., Frecer, V.: Ab initio studies of aromatic-aromatic and aromatic-polar interactions in the binding of substrate and inhibitor to dihydrofolate-reductase. *Int. J. Pept. Prot. Res*. **1992**, 39, 18-23. DOI: 10.1111/j.1399-3011.1992.tb01550.x

47 Frecer, V., Berti, F., Benedetti, F., Miertus, S.: Design of peptidomimetic inhibitors of aspartic protease of HIV-1 including –PheΨPro– core and favorable ADME properties. *J. Mol. Graph. Model.* **2008**, 27, 376-387.DOI: 10.1016/j.jmgm.2008.06.006

48 Frecer, V., Májeková, M., Miertus, S.: Approximate methods for the solvation of large biomolecules. *J. Mol. Struct. (Theochem)* **1989**, 52, 403-419.

49 Fischer, S.; Smith, J.C.; Verma, C. Dissecting the vibrational entropy change on protein/ligand binding: burial of a water molecule in bovine pancreatic trypsin inhibitor, *J. Phys. Chem.* B 105 (2001) 8050–8055.

50 Li, H.; Sutter, J.; Hoffmann, R. Pharmacophore Perception, Development and Use in Drug Design; Güner, O.F., Ed.; *International University Line*: La Jolla, CA, USA, **2000**, 171–189.

51 Xu, Y.; Goodacre, R. On splitting training and validation set: A comparative study of cross-validation, bootstrap and systematic sampling for estimating the generalization performance of supervised learning. *Journal of Analysis and Testing.* **2018**, 2, 249–262.

52 Supuran, C.T. Carbonic anhydrases: novel therapeutic applications for inhibitors and activators. *Nat.rev.- drug discov.*, **2008**, 7, 168-181. www.nature.com/reviews/ drugdisc.

53 Supuran, C.T. Structure-based drug discovery of carbonic anhydrase Inhibitors. *J. Enz. Inhib. Med. Chem*, **2012**, 27, 759–772. DOI: 10.3109/14756366.2012.672983

54 Temperini, C.; Innocenti, A.; Scozzafava, A.; Parkkila, S.; Supuran, C.T. The Coumarin-Binding Site in Carbonic Anhydrase Accommodates Structurally Diverse Inhibitors: The Antiepileptic Lacosamide As an Example and Lead Molecule for Novel Classes of Carbonic Anhydrase Inhibitors. *J. Med. Chem.* **2010**, 53, 850–854. DOI: 10.1021/jm901524f

55 Discovery Studio Molecular Modeling and Simulation Program, version 2.5; *Accelrys*, Inc.: San Diego, CA, USA, **2009**.

56 Alterio, V.; De Simone, G.; Monti, S.M.; Scozzafava, A.; Supuran, C.T. Carbonic anhydrase inhibitors: inhibition of human, bacterial, and archaeal isozymes with benzene-1,3-disulfonamides–solution and crystallographic studies. *Bioorg. Med. Chem. Lett.*, **2007**, 17, 4201–4207. DOI: 10.1016/j.bmcl.2007.05.045

57 N'Guessan, H.; Megnassan, E. In silico design of phosphonic arginine and hydroxamic acid inhibitors of Plasmodium falciparum M17 Leucyl aminopeptidase with favorable pharmacokinetic profile—2017. *J. Drug Des. Med. Chem.* **2017**, 3, 86–113.

58 Available Chemicals Directory, Version 95.1, MDL Information Systems, San Leandro, CA. 2003. Available online: http://cds3.dl.ac.uk/cds/cds.html (accessed on 13 August 2019).

59 Lipinski, C.A.; Lombardo, F.; Dominy, B.W.; Feeney, P.J. Experimental and computational approaches to estimate solubility and permeability in drug discovery and development settings. *Adv. Drug Deliv. Rev.* **2001**, 46, 3–26. DOI: 10.1016/s0169-409x(00)00129-0

60 Supuran, C.T, Exploring the multiple binding modes of inhibitors to carbonic anhydrases for novel drug discovery.*Expert opinion on drug discovery*, **2020**,15, 671-686. DOI : 10.1080/17460441.2020.1743676.

61 Maresca, A.; Temperini, C.; Pochet, L.; Masereel, B.; Scozzafava, A.; Supuran, C.T. Deciphering the mechanism of carbonic anhydrase inhibition with coumarins and thiocoumarins. *J. Med. Chem*, **2010**, 53, 335. DOI: 10.1021/jm901287j

62 Alterio, V.; Di Fiore, A.; D'Ambrosio, K.; Supuran, C.T.; De Simone, G. X-Ray crystallography of CA inhibitors and its importance in drug design. *In Drug Design of Zinc-Enzyme Inhibitors: Functional, Structural, and Disease Applications;* Supuran, C.T.; Winum, J. Y. Eds.; Wiley: Hoboken, **2009**, pp 73-138.

63 Liang, Z.; Xue, Y.; Behravan, G.; Jonsson, B.H.; Lindskog, S. Importance of the conserved active-site residues Tyr7, Glu106 and Thrl99 for the catalytic function of human carbonic anhydrase II; *Eur. J. Biochem.* **1993**, 211, 821-827. DOI: 10.1111/j.1432-1033.1993.tb17614.x

64 Xue, Y.; Liljas, A.; Jonsson, B.H.; Lindskog, S. Structural Analysis of the Zinc Hydroxide-Thr-199-Glu-106 Hydrogen-Bond Network in Human Carbonic Anhydrase II; *PROTEINS Structure, Function, and Genetics*. **1993**, 17, 93-106. DOI: 10.1002/prot.340170112

65 Merz, K. M. Jr. Insights into the Function of the Zinc hydroxide-Thrl99- Glu106 Hydrogen Bonding Network in Carbonic Anhydrases; *J. Mol. Biol.* **1990**, 21(4), 799-802. DOI: 10.1016/0022-2836(90)90333-H